Journal of Fusion Energy (2025) 44:65
https://doi.org/10.1007/s10894-025-00531-1

RESEARCH

Measurements of Optical Emission from Singly Ionized Er Ions at LHD for Laboratory Assessment of Atomic Data Relevant to Opacity of Kilonovae

Priti[1,2] · Motoshi Goto[1,3] · Tetsutaro Oishi[4] · Hiroyuki A. Sakaue[1] · Izumi Murakami[1,3] · Nobuyuki Nakamura[5] · Hajime Tanuma[6] · Masaomi Tanaka[7,8] · Gediminas Gaigalas[9] · Daiji Kato[1,10]

Received: 15 July 2025 / Accepted: 13 November 2025

Abstract
The atomic data of heavy elements, especially rare-earth metals, plays a crucial role in enhancing our understanding and interpreting kilonova spectra and underlying astrophysical processes. Among these elements, Erbium (Er) is particularly intriguing because it is important for opacities of the kilonova observed in 2017 (GW170817). In order to assess the atomic data, optical spectra of Er ions were precisely measured in $385 - 400\,\mathrm{nm}$ at Large Helical Device (LHD). In the present experiment, Er was injected into the core plasma of LHD through carbon pellets containing Er powders. The electron density and temperature of the Er-contained C pellet ablation cloud were obtained to be $1.6 \times 10^{22}\,\mathrm{m}^{-3}$ and 1.4 eV using the Stark broadening of a C II line and the Boltzmann plot of Er II lines, respectively. Transition probabilities of observed Er II lines were assessed using the Boltzmann plot analysis. Recent measurements with laser-induced breakdown spectroscopy (LIBS) of an Er II line at 393.86 nm were confirmed by the present work.

Keywords Lanthanide · Opacity · Kilonova

Introduction

Understanding the origin and evolution of heavy elements in the universe is a central question in astrophysics, and kilonovae [1, 2] –explosive events resulting from the merger of neutron stars– are now recognized as major sites for rapid neutron-capture (r-process) nucleosynthesis. The optical and near-infrared spectra emitted by ejecta from the merger, carry crucial information about the composition, temperature, and velocity of the ejected material. Such kilonova was actually observed following the detection of gravitational waves in 2017 (GW170817) [3, 4].

The emission from the kilonova is delayed and dimmer if heavy *r*-process elements such as lanthanide and actinide

✉ Daiji Kato
kato.daiji@nifs.ac.jp

1 National Institute for Fusion Science, National Institutes of Natural Sciences, Toki, Gifu 509-5292, Japan

2 Present address: P.G. Department of Physics, Magadh University, Bodhgaya, Bihar 824234, India

3 Department of Fusion Science, Sokendai, Toki, Gifu 509-5292, Japan

4 Department of Quantum Science and Energy Engineering, Graduate School of Engineering, Tohoku University, Sendai, Miyagi 980-8579, Japan

5 Institute for Laser Science, The University of Electro-Communications, Chofu, Tokyo 182-8585, Japan

6 Department of Physics, Tokyo Metropolitan University, Hachioji, Tokyo 192-0397, Japan

7 Astronomical Institute, Tohoku University, Sendai, Miyagi 980-8578, Japan

8 Division for the Establishment of Frontier Sciences, Organization for Advanced Studies, Tohoku University, Sendai, Miyagi 980-8577, Japan

9 Institute of Theoretical Physics and Astronomy, Faculty of Physics, Vilnius University, Saulėtekio 3, 10257 Vilnius, Lithuania

10 Interdisciplinary Graduate School of Engineering Sciences, Kyushu University, Kasuga, Fukuoka 816-8580, Japan

Published online: 02 December 2025

(open *f*-shell) are abundant in the ejecta due to their high opacities [e.g., 5, 6]. In fact, the observed light curves of optical and infra-red counterpart to GW170817 confirm the existence of some lanthanide contents in the ejecta [e.g., 7, 8, 9, 10, 11]. There are numerous works [e.g., 7, 12, 13, 14, 15, 16, 17, 18, 19, 20, 21, 22] of atomic structure calculations for lanthanide elements to follow up the opacity evaluation with complete and more accurate atomic data.

However, interpreting the spectral features of the kilonova still remains a challenge due to uncertainty in the theoretical atomic data for the lanthanide series. Laboratory measurements of atomic data such as wavelengths, energy levels, and transition probabilities are, therefore, indispensable for validating theoretical atomic structure and opacity calculations.

Erbium (Er) in low-temperature plasmas stands out as important due to its significant contribution to the opacity of the kilonova [14, 20, 21]. In the NIST Atomic Spectral Database (ASD) [23], 502 lines of Er I and II for optical wavelengths are registered on the basis of the data compilation by Meggers et al. [24] in 1975. However, most of them are listed without energy level identifications and transition probabilities. Meanwhile, as for Er II, many works have been done for energy level identification and laboratory measurements of transition probabilities [25–34].

To contribute to this, we have carried out laboratory measurements of optical spectra from erbium ions utilizing spectroscopy and pellet injection systems installed for fusion plasma diagnostics at Large Helical Device (LHD). In present experiments, Er was introduced into the core plasma using carbon pellets embedded with Er powders. The resulting emission spectra from the ablation cloud were measured in the $385 - 400$ nm range with a high-resolution UV-visible spectrometer, where distinct spectral lines from Er II and C II ions were clearly identified. In particular, the transition probability of the prominent Er II line at 393.86 nm was assessed using Boltzmann plot analysis, adding a benchmark for evaluating theoretical atomic data relevant to astrophysical opacity models.

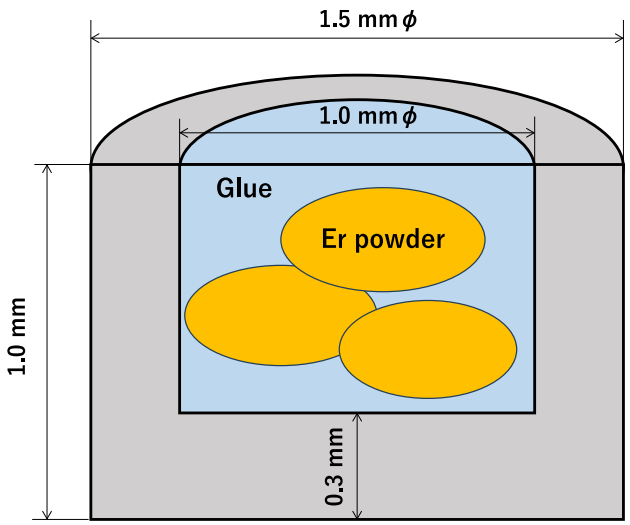

Fig. 1 Schematic of the graphite pellet containing erbium powders

This paper is structured as follows: Section Brief description of Er/C Pellet injection experiment in LHD describes the experimental setup for the Er/C pellet injection in the LHD. Section Results and discussion presents the results of the optical emission measurements from the ablation cloud. In Sections Observed Pellet ablation cloud optical spectra to Boltzmann plot analysis of Er II lines, we detail the spectral line identification, analyze the emission features, and estimate the transition probability of Er II using the Boltzmann plot method. In Section Summary, we summarize the findings.

Brief Description of Er/C Pellet Injection Experiment in LHD

Pellet Injection

In LHD, a torus-shape plasma with the major radius of about 3.9 m and the minor radius of about 0.6 m (the typical plasma volume is about $30\,\mathrm{m}^3$) is magnetically confined. The major radius position of the magnetic axis is 3.6 m and the field strength at the magnetic axis is 2.54 T. The plasma of hydrogen gas was obtained by electron cyclotron resonance heating followed by neutral beam injection. The line averaged electron density and the electron temperature at the plasma center were about $1 \times 10^{19}\,\mathrm{m}^{-3}$ and 3 keV, respectively.

We used a cylindrical graphite pellets (1.5 mm diameter and 1.0 mm length) containing erbium powders. The erbium powder was packed into a hollow (1.0 mm diameter and 0.7 mm depth) made at the center of the graphite cylinder and secured with cyanoacrylate glue (ThreeBond TB1757) as illustrated in Figure 1. The pellets were injected from the outer port (10-O) of LHD using a pneumatic pipe-gun system with 10–20 atm pressure helium gas [35]. The pellet surface will be ablated as soon as injected into the plasma by a high heat flux from the background plasma. A high-density ablation cloud is formed and kept at low temperatures (a few eV) as the heat flux is balanced with energy consumption rates due to ablation and subsequent atomic processes such as radiation and ionization. A physics model of the pellet ablation is detailed in [36].

Figure 2 shows the portion of the equatorial plane of the pellet injection port and the observation port. The line of sight intersects the track of the pellet ablation cloud in the plasma. Since the typical speed of the injected pellet is about 200 m/s, we can observe photon emissions from the

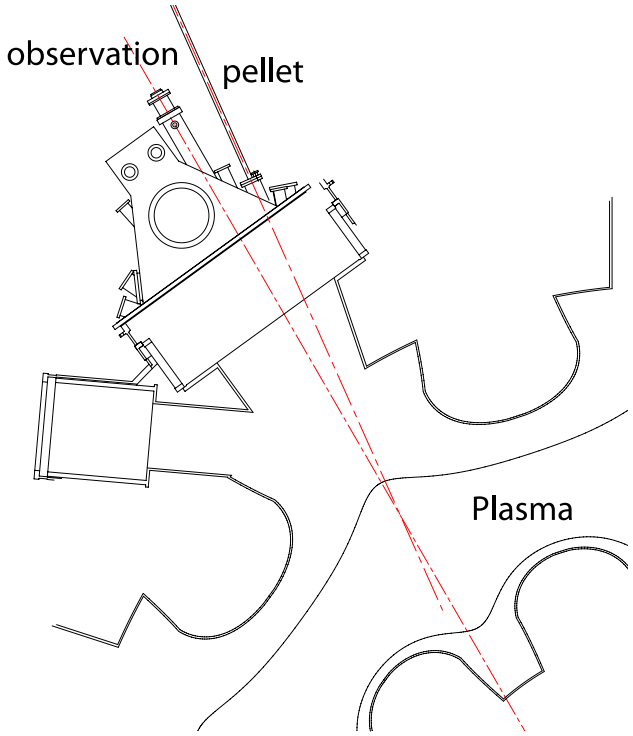

Fig. 2 A top view of the equatorial plane of the pellet injection port and the observation port

pellet ablation cloud passing through the field of view (a few cm long) in about 100 μs. In such a short time, emission from the background plasma can be neglected. This enabled us to take a snap shot of the strong emission from the ablation cloud.

Observation System

Photons from the ablation cloud were detected during the exposure time of 5 ms through optical fibers placed at the observation port (Figure 2). The optical fibers with core and clad diameters of 100 and 125 μm, respectively, were used [37]. An optical lens with the focal length of 3 cm is attached to the fiber giving a narrow field of view (3 cm at the plasma center). The other end of the fiber is located in front of the entrance of a Czerny–Turner visible-UV spectrometer (the focal length of 50 cm) [38] equipped with a CCD detector. For the present measurements, the entrance slit width was 20 μm, and the grating of 1800 gr/mm was used. The instrumental function measured with the line at 435.833 nm from a mercury lamp using the slit width of 25 μm is approximated by the Gaussian full width at half maximum (FWHM) of 0.036 nm. Thus, the instrumental FWHM of the present measurements with the narrower slit width (20 μm) should be smaller than 0.036 nm. The wavelength-dependent sensitivity calibration of the spectrometer was performed with an integrating sphere using the same optical system as the actual measurement.

Results and Discussion

Observed Pellet Ablation Cloud Optical Spectra

This section presents the results of the spectroscopic measurements. The identification of charge states and corresponding transitions was carried out using data from the NIST Atomic Spectra Database [23]. The spectra obtained from the carbon pellet and the Er-contained carbon pellet are shown in Figures 3(a) and (b), respectively. In Figure 3(a), most of the prominent spectral lines are attributed to C II/III and O II ions, whereas Figure 3(b) shows the line-integrated intensities of the Er II lines in addition to the lines of C and O. The O lines originate from the cyanoacrylate glue of the pellet. Wavelength calibration was performed using reference lines of C II/III and O II indicated in Figure 3(a). The central wavelength of each peak was obtained by fitting to the Gaussian profile. The uncertainty in wavelength calibration, estimated from the residuals of the quadratic calibration curve, is approximately 0.02 nm. Wavelengths of the Er II lines determined in the present experiment (see Table 1) agree with those reported in the previous works by Lawler et al. [29] and Wyart et al. [30].

Electron Density of Ablation Cloud from Line Shape Fitting of Observed C II Lines

As shown in Figure 3, the strong emission lines from C II ions are observed along with Er II transitions in the ablation cloud. Several of these line profiles are likely to exhibit Stark broadening, which can be used to determine the electron density (n_e). To estimate n_e in the present ablation cloud plasma, we focus on the Stark broadening analysis of the C II line at 392.06 nm of the $4s \rightarrow 3p_{3/2}$ transition.

The overall line shape is represented by the Voigt profile, obtained by convolving the Lorentzian (Stark broadening) and Gaussian (Doppler broadening and Instrumental function) distribution functions, which is expressed as

$$y(\lambda) = y_0 + \frac{A \cdot 2\ln(2) \cdot w_L}{\pi^{3/2} w_G^2} \int_{-\infty}^{\infty} \frac{\exp(-t^2)}{\left(\frac{\sqrt{\ln(2)} \cdot w_L}{w_G}\right)^2 + \left(\frac{\sqrt{4\ln(2)}(\lambda - \lambda_c)}{w_G} - t\right)^2} dt, \quad (1)$$

where y(λ) is Voigt profile intensity at position λ, y_0 background offset, A area under the curve, w_L Lorentzian

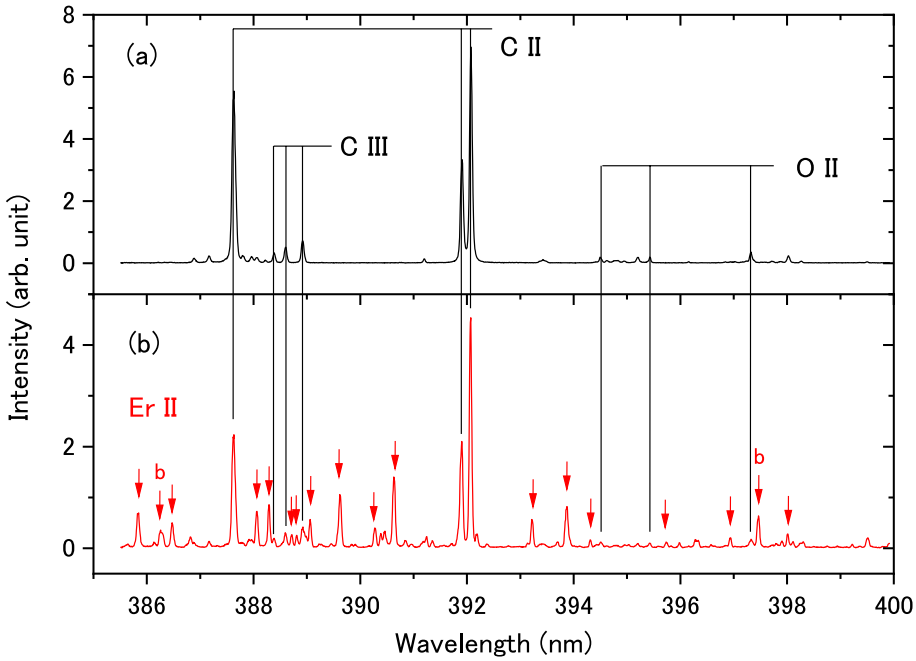

Fig. 3 Line-integrated intensities of pellet ablation cloud spectra. (a) is for the spectrum of the C pellet (LHD shot number 176174), and (b) for the spectrum of the Er-contained C pellet (LHD shot number 176176). The reference lines of C II/III and O II used for wavelength calibration are indicated. In (b), the Er II lines are identified by red arrows. "b" stands for blended lines

Table 1 Wavelengths and relative line intensities for the Boltzmann plot. A_{ij} values are taken from Lawler (2008) [29], except for three lines at 388.81 nm, 393.22 nm, and 395.73 nm from Wyart (2009) [30]

λ (nm)	I	Lower Level			Upper Level			A_{ij} (10^7 s^{-1})
		E_j(eV)	$2J_j$	Parity	E_i (eV)	$2J_i$	Parity	
385.83	0.55	0.89211	9	even	4.10456	11	odd	1.85(9)
386.47	0.36	1.35067	7	even	4.55780	9	odd	2.33(14)
388.06	0.49	0.63636	9	even	3.83042	7	odd	3.13(16)
388.28	0.52	0.88644	11	even	4.07862	9	odd	3.16(16)
388.71	0.18	1.36911	9	even	4.55780	9	odd	1.01(7)
388.81	0.16	0	13	even	3.18791	15	odd	0.14
389.06	0.34	na	na	na	na	na	na	na
389.62	0.79	0.05460	11	even	3.23586	13	odd	2.39(12)
390.27	0.28	0.89211	9	even	4.06804	11	odd	0.88(4)
390.63	1.00	0	13	even	3.17304	11	odd	4.82(24)
393.22	0.35	0.63636	9	even	3.78847	7	odd	1.83
393.86	0.63	0	13	even	3.14701	11	odd	na
394.31	0.09	0.88644	11	even	4.02981	9	odd	0.338(19)
395.73	0.09	2.28916	15	odd	5.42120	17	even	0.59
396.93	0.14	0.63636	9	even	3.75894	9	odd	0.296(22)
398.01	0.18	0.88644	11	even	4.00062	9	odd	0.313(18)

FWHM, w_G Gaussian FWHM, λ_c central wavelength, and t dummy variable for convolution integration.

Additionally, due to the presence of a strong magnetic field in the LHD plasma, Zeeman splitting must be taken into account. The Zeeman splitting for each fine structure level was calculated using the HFSZEEMAN95 package [39]. The splitting is consistent with the Landé g factors available in NIST ASD [23]. The spectral line is modeled as the sum of multiple Zeeman components, each characterized by a specific wavelength shift for the magnetic field strength of 2.0 T and the relative intensity for observing perpendicular to the magnetic field lines. The best fit to the C II line is obtained for $w_L = 0.012$ nm and $w_G = 0.033$ nm, as shown in Figure 4.

Another peak at 391.89 nm is assigned to the C II line of the $4s \rightarrow 3p_{1/2}$ transition. However, there is blending with weak lines at the shorter wavelength side of the peak. Therefore, we omitted this peak from the present analysis.

Figure 5 shows the Stark broadening of the C II lines as a function of electron densities. The experimental data taken from Goly and Weniger [40] and Roberts and Ecker [41] for the C II lines show a linear dependence on the electron densities. The theoretical Stark broadening calculated using the flexible atomic code (FAC) [42] which

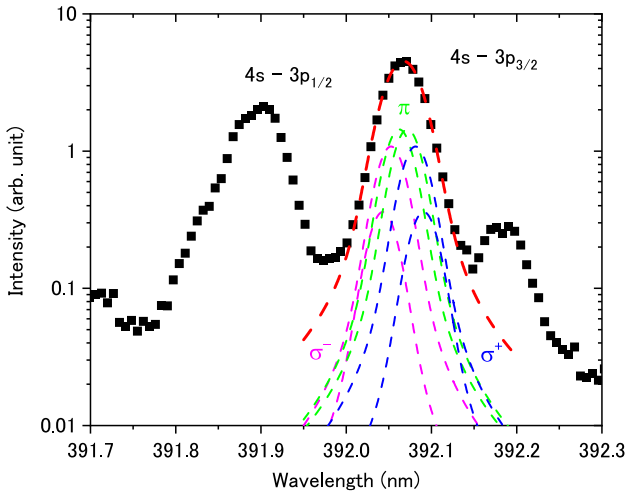

Fig. 4 Emission line profile of the C II $4s \rightarrow 3p_{1/2}$ and $4s \rightarrow 3p_{3/2}$ lines measured for the ablation cloud of the Er-contained C pellet (solid squares). The profiles are fitted with Voigt functions for individual Zeeman components, corresponding to a magnetic field strength of 2.0 T

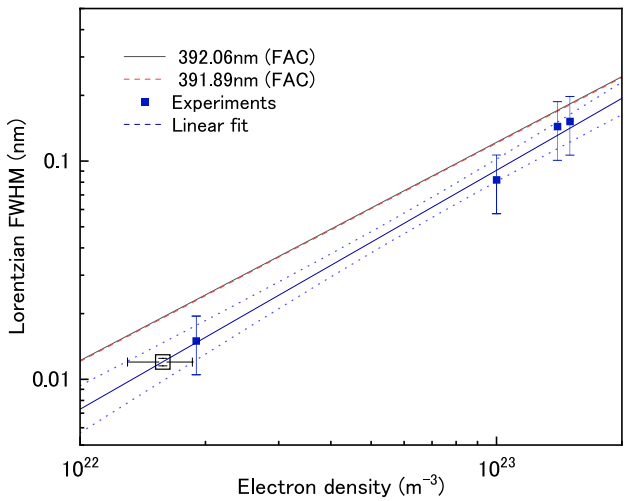

Fig. 5 Stark broadening widths of the C II $4s \rightarrow 3p_{1/2}$ and $4s \rightarrow 3p_{3/2}$ lines plotted as a function of electron density (n_e). Experimental data from Goly and Weniger [40] and Roberts and Ecker [41] are plotted by solid squares. The dashed line shows the linear fit, with the 95% confidence interval indicated by the dotted lines, which is used for an estimate of the electron density in the present study. Theoretical results are obtained by using flexible atomic code (FAC) [42]. Black circle represents the present results and vertical error bar of black circle represent the uncertainty in the Voigt fitting and horizontal error bar indicate the uncertainty of the electron density deduced with the confidence interval of 95%

almost coincides for both of the C II lines, overestimates the experimental values. For the Lorentzian FWHM of the C II line ($w_L = 0.012\,\mathrm{nm}$), the electron density is estimated to be $(1.6 \pm 0.3) \times 10^{22}\,\mathrm{m}^{-3}$. The temperature dependence of Stark broadening is known to be weak in the range of $1 - 5$ eV and is, therefore, neglected in this analysis.

Goto et al. [38] obtained a factor of 4 larger density using the broadening of C II $3d \rightarrow 3p$ at 723 nm from a C pellet ablation cloud. This discrepancy may arise from differences in the composition of the pellets and the plasma conditions. In any case, the electron density of the LHD ablation cloud ($\sim 10^{22}\,\mathrm{m}^{-3}$) is higher than the McWhirter criterion [43, 44],

$$n_e \geq 1.6 \times 10^{18} (T_e)^{1/2} (\Delta E)^3, \tag{2}$$

which gives a minimum density required to approximate excited-level populations by the Boltzmann distribution. n_e, T_e, and ΔE are expressed in m^{-3}, K, and eV, respectively. Thus, we apply the Boltzmann plot analysis for transition probabilities as explained in the next section.

It is noted that for optically thin plasmas such that self-absorption effects are negligible, line intensities of transitions originated from the same upper level are proportional to their respective spontaneous emission probabilities. The observed intensity ratio of the two C II lines, corresponding to the $4s \rightarrow 3p_{3/2}$ and $4s \rightarrow 3p_{1/2}$ transitions, respectively, is 1.82 ± 0.06. This value is in good agreement with the corresponding ratio of transition probabilities, 1.85 ± 0.26, as reported in the NIST database [23]. Therefore, the self-absorption effects are not taken into account in the present analysis.

Since the Debye length in the ablation cloud is much larger comparing with atomic size, plasma density effects (screening effects) to atomic energy levels and transition probabilities can also be neglected.

Boltzmann Plot Analysis of Er II Lines

The intensity I_{ij} of an emission line (i. e., the photon emission rate) for a transition from the upper level *i* to the lower level *j* is proportional to the population of the upper energy level multiplied by the transition probability A_{ij}. Assuming the Boltzmann distribution of the upper-level populations at an electron temperature T_e, the line intensity can be expressed as

$$I_{ij} = g_i A_{ij} \cdot C \cdot \exp\left(-\frac{E_i}{kT_e}\right) \tag{3}$$

where g_i is the statistical weight of the upper level, E_i is the excitation energy of the upper level, k is the Boltzmann constant, and C is a constant that depends on the ion species and overall plasma parameters. Taking the natural logarithm of both sides gives

$$\ln\left(\frac{I_{ij}}{g_i A_{ij}}\right) = -\frac{E_i}{kT_e} + C \tag{4}$$

Therefore, $\ln(I_{ij}/g_iA_{ij})$ and E_i are expected to show a linear relationship if the upper-level populations follow the Boltzmann distribution. The slope of this line is equal to $-1/(kT_e)$, allowing the estimation of the T_e and from the $\ln(I_{ij}/g_iA_{ij})$ values the unknown transition probability can be evaluated. Recently, the same scheme was applied with laser-induced breakdown spectroscopy (LIBS) to obtain unknown transition probabilities of lanthanide ions [33, 34, 45].

The Er II lines used for the present analysis are summarized in Table 1, along with their corresponding transition probabilities and details of the upper and lower energy levels. The relative intensity I_{ij} of measured peak was obtained by fitting to a Gaussian function. We removed the blended lines (see Figure 3) from the plot due to a large uncertainty in the deduced intensities. Although the strong line observed at 389.06 nm can be assigned to Er II [23], this line is not useful for the analysis because no information on the energy level is available. The two lines at 386.47 nm and 388.71 nm of the same upper level at 4.5578 eV have the intensity ratio of 2.07 ± 0.08 which is consistent with the branching ratio of their transition probabilities (2.3 ± 0.2), indicating negligible self-absorption effects as in the case of the C II lines analyzed in the previous section.

Figure 6 shows the Boltzmann plot of $\ln(I_{ij}/g_iA_{ij})$ for the lines listed in Table 1 along the upper-level energy (E_i) of each transition. The error bars reflect uncertainties arising from (i) statistical uncertainty in the Gaussian fitting for the relative intensity, and (ii) uncertainty of the A_{ij} values. Although the data points are scattered, a negative correlation between $\ln(I_{ij}/g_iA_{ij})$ and E_i is apparent, indicating that higher energy levels are less populated. A linear fit to the data weighted by the uncertainty is shown as the solid line in the figure. The dashed curves represent the 95% confidence interval of the fit. The T_e deduced from the slope of the fitted line is 1.4 ± 0.3 eV. This value is similar to that obtained from Al II lines of an Al pellet ablation cloud at LHD (1.51 ± 0.04 eV [46]), whereas it is significantly lower than that obtained from the C II line of the C pellet ablation cloud (2.5 eV [38]).

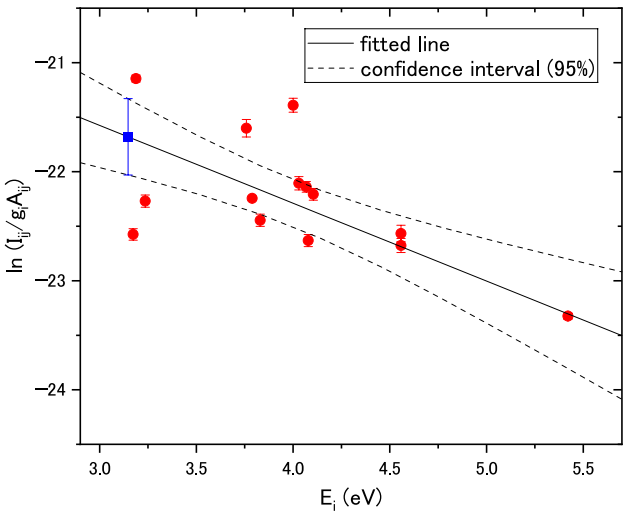

Fig. 6 Boltzmann plot obtained using the present experimental line intensity I_{ij} and the A_{ij} values from Lawler et al. [29] and Wyart et al. [30] (red circles). The solid line is obtained by linear fitting of the experimental data accounting for uncertainties of each data. The blue square indicates the value at 3.147 eV used to determine the A_{ij} value for the Er II line at 393.86 nm. The dashed curves indicate the confidence interval of 95%

In the present measurements, the peak intensity at 387.62 nm for the Er-contained C pellet (Figure 3(b)) is apparently decreased relative to the two peaks of C II lines around 392 nm as compared with the case of the C pellet (Figure 3(a)). The peak at 387.62 nm is due to emission lines from the $2s\ 2p\ 4f$ levels which have higher energies than the upper level of the two lines around 392 nm, $2s^2\ 4s$. Populations of the $2s\ 2p\ 4f$ levels and the emission line intensity will, therefore, decrease at lower temperatures, provided that the Boltzmann distribution is applied. Thus, a lower temperature is inferred for the Er-containing C pellet than the C pellet, which may be explained by a larger radiation cooling rate expected with the existence of Er.

It is noted that doubly ionized Er ions would also have a large fractional abundance at this temperature, as predicted using the Saha ionization formula. Nevertheless, the Er III lines in $385 - 400$ nm can not be observed because their gA values reported by Wyart et al. [47] are two orders of magnitude smaller than those of the strong Er II lines.

The emission line at 393.86 nm is of particular interest in this study because the transition probability has not yet been determined. Although the NIST Atomic Spectra Database [23] provides the upper and lower level for this transition as an excited level at 3.147 eV ($J = 11/2$) and the ground state level of $4f^{12}\ 6s$ ($J = 13/2$), respectively, no value for the transition probability is reported. Likewise, this line is not included in the extensive compilation of Er II transition probabilities by Lawler et al. [29]. Wyart et al. [30] and Ankush et al. [32] have assigned the upper level primarily to the $4f^{11}\ 5d\ 6s$ configuration, noting significant mixing from $4f^{11}\ 6s^2, 4f^{12}\ 6p$, and $4f^{11}\ 5d^2$ configurations. To date, there are two measurements for the transition probability using LIBS reported by Naoi et al. [33] and Irvine et al. [34]. However, *ab-initio* calculation of the transition probability remains highly uncertain.

In this work, the transition probability for the target line at 393.86 nm was estimated by using the Boltzmann plot at its known upper-level energy (blue square in Figure 6). This gives the value of $(1.24 \pm 0.43) \times 10^7\ \mathrm{s}^{-1}$ which is consistent with the values obtained by Naoi et al. [33] and Irvine et al. [34] using LIBS (see Table 2). The uncertainty in Naoi's estimated value is mainly due to the confidence

Table 2 Summary of the upper and lower energy levels, and transition probability data for the Er II line at 393.86 nm

	Upper level	Lower Level	A_{ij} (10^7 s^{-1})
	$4f^{11}$ $5d$ $6s$ $(J = 11/2)$	$4f^{12}$ $6s$ $(J = 13/2)$	
Present work			1.24(43)
Naoi et al. [33]			1.2(2)
Irvine et al. [34]			1.51(57)

interval with 68.3% of the linear fit in the Boltzmann plot. In the present result, however, we used the larger confidence interval of 95% because smaller number of data points are available for the Boltzmann plot. The deviation from the value of Irvine et al. [34] is larger, nevertheless it falls into the confidence interval.

Summary

Experimentally deriving the transition probabilities for lines of lanthanide ions are crucial not only for enhancing the accuracy and completeness of atomic databases but also for validating complex atomic structure calculations. Given the intricacy of the lanthanide spectra, particularly the strong interactions among *f*, *d*, and *p* orbitals, theoretical predictions are inherently challenging and prone to uncertainty. Therefore, reliable experimental values are essential, especially for applications in astrophysical contexts such as kilonovae, where the lanthanide ions contribute significantly to its opacity.

In the present work, we performed the optical spectral measurement of singly charged Er ions and assessment of the transition probabilities relevant to the kilonova of the neutron star merger utilizing the spectroscopy and pellet injection systems developed for magnetically confined fusion plasma at the LHD.

Transition probabilities of the Er II lines in $385 - 400\,\mathrm{nm}$ were assessed using the Boltzmann plot analysis. For validity of our analysis assuming the Boltzmann distribution of excited-level population, the Stark broadening of the C II line at 392.06 nm was measured accounting for the Zeeman splitting at 2 T. The electron density and temperature of the Er-contained C pellet ablation cloud are deduced to be about $1.6 \times 10^{22}\,\mathrm{m}^{-3}$ and 1.4 eV, respectively, justifying the Boltzmann distribution of the excited-level population. The transition probability of the Er II line at 393.86 nm was particularly investigated in this study because this transition probability has not been determined and accurate *ab-initio* calculations are difficult. The present work confirmed the transition probabilities obtained recently with LIBS [33, 34]. The results of this study serve to verify the validity of benchmarking experimental data.

Acknowledgements This work is supported by the NIFS collaboration programs (NIFS22KIIF005, NIFS24KIIQ013). Priti is grateful to NIFS for her COE research fellowship $(2021 - 2023)$. The authors thank the LHD Experiment Group for their excellent cooperation.

Author Contributions D.K. and P.P. wrote the main manuscript text. M.G., T.O. and H.A.S. contributed experimental preparation and implementation. All authors reviewed the manuscript.

Data Availability Data is provided within the manuscript.

Declarations

Competing interests The authors declare no competing interests.

References

1. L.-X. Li, B. Paczyński, Transient events from neutron star mergers. The Astrophysical Journal Letters **507**, 59–62 (1998). https://doi.org/10.1086/311680. arXiv:astro-ph/9807272
2. B.D. Metzger, G. Martínez-Pinedo, S. Darbha, E. Quataert, A. Arcones, D. Kasen, R. Thomas, P. Nugent, I.V. Panov, N.T. Zinner, Electromagnetic counterparts of compact object mergers powered by the radioactive decay of r-process nuclei. Mon. Not. R. Astron. Soc. **406**, 2650–2662 (2010). https://doi.org/10.1111/j.1365-2966.2010.16864.x. arXiv:1001.5029 [astro-ph.HE]
3. B.P. Abbott, R. Abbott, T.D. Abbott, F. Acernese, K. Ackley, C. Adams, T. Adams, P. Addesso, R.X. Adhikari, V.B. Adya et al., GW170817: observation of Gravitational Waves from a Binary Neutron Star Inspiral. Phys. Rev. Lett. **119**(16), 161101 (2017). https://doi.org/10.1103/PhysRevLett.119.161101. arXiv:1710.05832 [gr-qc]
4. B.P. Abbott, R. Abbott, T.D. Abbott, F. Acernese, K. Ackley, C. Adams, T. Adams, P. Addesso, R.X. Adhikari, V.B. Adya et al., Multi-messenger observations of a binary neutron star merger. The Astrophysical Journal Letters **848**, 12 (2017). https://doi.org/10.3847/2041-8213/aa91c9. arXiv:1710.05833 [astro-ph.HE]
5. D. Kasen, N.R. Badnell, J. Barnes, Opacities and spectra of the r-process ejecta from neutron star mergers. Astrophys. J. **774**, 25 (2013). https://doi.org/10.1088/0004-637X/774/1/25. arXiv:1303.5788 [astro-ph.HE]

6. M. Tanaka, K. Hotokezaka, Radiative transfer simulations of neutron star merger ejecta. Astrophys. J. **775**, 113 (2013). https://doi.org/10.1088/0004-637X/775/2/113. arXiv:1306.3742 [astro-ph.HE]
7. D. Kasen, B. Metzger, J. Barnes, E. Quataert, E. Ramirez-Ruiz, Origin of the heavy elements in binary neutron-star mergers from a gravitational-wave event. Nature **551**, 80–84 (2017). https://doi.org/10.1038/nature24453. arXiv:1710.05463 [astro-ph.HE]
8. M. Tanaka, Y. Utsumi, P.A. Mazzali, N. Tominaga, M. Yoshida, Y. Sekiguchi, T. Morokuma, K. Motohara, K. Ohta, K.S. Kawabata, F. Abe, K. Aoki, Y. Asakura, S. Baar, S. Barway, I.A. Bond, M. Doi, T. Fujiyoshi, H. Furusawa, S. Honda, Y. Itoh, M. Kawabata, N. Kawai, J.H. Kim, C.-H. Lee, S. Miyazaki, K. Morihana, H. Nagashima, T. Nagayama, T. Nakaoka, F. Nakata, R. Ohsawa, T. Ohshima, H. Okita, T. Saito, T. Sumi, A. Tajitsu, J. Takahashi, M. Takayama, Y. Tamura, I. Tanaka, T. Terai, P.J. Tristram, N. Yasuda, T. Zenko, Kilonova from post-merger ejecta as an optical and near-infrared counterpart of GW170817. Publ. Astron. Soc. Jpn. **69**, 102 (2017). https://doi.org/10.1093/pasj/psx121. arXiv:1710.05850 [astro-ph.HE]
9. A. Perego, D. Radice, S. Bernuzzi, AT 2017gfo:an anisotropic and three-component kilonova counterpart of GW170817. The Astrophysical Journal Letters **850**, 37 (2017). https://doi.org/10.3847/2041-8213/aa9ab9. arXiv:1711.03982 [astro-ph.HE]
10. S. Rosswog, J. Sollerman, U. Feindt, A. Goobar, O. Korobkin, R. Wollaeger, C. Fremling, M.M. Kasliwal, The first direct double neutron star merger detection: implications for cosmic nucleosynthesis. Astronomy & Astrophysics **615**, 132 (2018). https://doi.org/10.1051/0004-6361/201732117. arXiv:1710.05445 [astro-ph.HE]
11. K. Kawaguchi, M. Shibata, M. Tanaka, Radiative transfer simulation for the optical and near-infrared electromagnetic counterparts to GW170817. The Astrophysical Journal Letters **865**, 21 (2018). https://doi.org/10.3847/2041-8213/aade02. arXiv:1806.04088 [astro-ph.HE]
12. M. Tanaka, D. Kato, G. Gaigalas, P. Rynkun, L. Radžiūtė, S. Wanajo, Y. Sekiguchi, N. Nakamura, H. Tanuma, I. Murakami, H.A. Sakaue, Properties of kilonovae from dynamical and post-merger ejecta of neutron star mergers. Astrophys. J. **852**(2), 109 (2018). https://doi.org/10.3847/1538-4357/aaa0cb
13. G. Gaigalas, D. Kato, P. Rynkun, L. Radžiūtė, M. Tanaka, Extended Calculations of Energy Levels and Transition Rates of Nd II-IV Ions for Application to Neutron Star Mergers. Astrophys. J. Suppl. Ser. **240**(2), 29 (2019). https://doi.org/10.3847/1538-4365/aaf9b8. arXiv:1901.10671 [astro-ph.SR]
14. M. Tanaka, D. Kato, G. Gaigalas, K. Kawaguchi, Systematic opacity calculations for kilonovae. Mon. Not. R. Astron. Soc. **496**(2), 1369–1392 (2020). https://doi.org/10.1093/mnras/staa1576. arXiv:1906.08914 [astro-ph.HE]
15. L. Radžiūtė, G. Gaigalas, D. Kato, P. Rynkun, M. Tanaka, Extended calculations of energy levels and transition rates for singly ionized lanthanide elements. I. Pr-Gd. Astrophys. J. Suppl. Ser. **248**(1), 17 (2020). https://doi.org/10.3847/1538-4365/ab8312. arXiv:2002.08075 [physics.atom-ph]
16. L. Radžiūtė, G. Gaigalas, D. Kato, P. Rynkun, M. Tanaka, Extended calculations of energy levels and transition rates for singly ionized lanthanide elements. II. Tb-Yb. Astrophys. J. Suppl. Ser. **257**(2), 29 (2021). https://doi.org/10.3847/1538-4365/ac1ad2
17. C.J. Fontes, C.L. Fryer, A.L. Hungerford, R.T. Wollaeger, O. Korobkin, A line-binned treatment of opacities for the spectra and light curves from neutron star mergers. Mon. Not. R. Astron. Soc. **493**(3), 4143–4171 (2020). https://doi.org/10.1093/mnras/staa485. arXiv:1904.08781 [astro-ph.HE]
18. C.J. Fontes, C.L. Fryer, R.T. Wollaeger, M.R. Mumpower, T.M. Sprouse, Actinide opacities for modelling the spectra and light curves of kilonovae. Mon. Not. R. Astron. Soc. **519**(2), 2862–2878 (2023). https://doi.org/10.1093/mnras/stac2792. arXiv:2209.12759 [astro-ph.HE]
19. A. Flörs, R.F. Silva, J. Deprince, H. Carvajal Gallego, G. Leck, L.J. Shingles, G. Martínez-Pinedo, J.M. Sampaio, P. Amaro, J.P. Marques, S. Goriely, P. Quinet, P. Palmeri, M. Godefroid, Opacities of singly and doubly ionized neodymium and uranium for kilonova emission modeling. Mon. Not. R. Astron. Soc. **524**(2), 3083–3101 (2023). https://doi.org/10.1093/mnras/stad2053. arXiv:2302.01780 [astro-ph.HE]
20. D. Kato, M. Tanaka, G. Gaigalas, L. Kitovienė, P. Rynkun, Systematic opacity calculations for kilonovae - II. Improved atomic data for singly ionized lanthanides. Mon. Not. R. Astron. Soc. **535**(3), 2670–2686 (2024). https://doi.org/10.1093/mnras/stae2504. arXiv:2501.13286 [astro-ph.HE]
21. J. Deprince, H. Carvajal Gallego, S. Ben Nasr, L. Maison, J.-C. Pain, P. Palmeri, P. Quinet, Radiative and opacity data obtained from large-scale atomic structure calculations and from statistical simulations for the spectral analysis of kilonovae in their photospheric and nebular phases: the sample case of er iii. The European Physical Journal D **78**, 105 (2024). https://doi.org/10.1140/epjd/s10053-024-00897-5
22. J. Deprince, G. Wagle, S. Ben Nasr, H. Carvajal Gallego, M. Godefroid, S. Goriely, O. Just, P. Palmeri, P. Quinet, S. Van Eck, Kilonova ejecta opacity inferred from new large-scale hfr atomic calculations in all elements between ca (z = 20) and lr (z = 103). A&A **696**, 32 (2025). https://doi.org/10.1051/0004-6361/202452967
23. Kramida, A., Ralchenko, Y., Reader, J., NIST ASD Team (2024): NIST Atomic Spectra Database (version 5.12), [online]. (2025) https://doi.org/10.18434/T4W30F
24. W.F. Meggers, C.H. Corliss, B.F. Scribner, Tables of spectral-line intensities, part I – arranged by elements, in *National Bureau of Standards Monograph*, vol. 145, (U.S. Government Printing Office, Washington, DC, USA, 1975)
25. K. Musiol, S. Labuz, Experimental determination of the transition probabilities in er ii. Phys. Scr. **27**(6), 422 (1983). https://doi.org/10.1088/0031-8949/27/6/008
26. S.M. Bentzen, U. Nielsen, O. Poulsen, Lifetime measurements in singly ionized erbium using fast-beam laser-modulation spectroscopy. J. Opt. Soc. Am. **72**(9), 1210–1212 (1982). https://doi.org/10.1364/JOSA.72.001210
27. H. Xu, Z. Jiang, Z. Zhang, Z. Dai, S. Svanberg, P. Quinet, E. Biémont, Radiative lifetime measurements in er ii by time-resolved laser spectroscopy. J. Phys. B, At. Mol. Opt. Phys. **36**(9), 1771 (2003). https://doi.org/10.1088/0953-4075/36/9/309
28. M.H. Stockett, E.A. Den Hartog, J.E. Lawler, Radiative lifetimes for 80 levels of singly ionized erbium. J. Phys. B, At. Mol. Opt. Phys. **40**(23), 4529 (2007). https://doi.org/10.1088/0953-4075/40/23/012
29. J.E. Lawler, C. Sneden, J.J. Cowan, J.-F. Wyart, I.I. Ivans, J.S. Sobeck, M.H. Stockett, E.A. Den. Hartog, Improved laboratory transition probabilities for er ii and application to the erbium abundances of the sun and five r-process-rich, metal-poor stars. Astrophys. J. Suppl. Ser. **178**(1), 71 (2008). https://doi.org/10.1086/589834
30. J.-F. Wyart, J.E. Lawler, Theoretical interpretation and new energy levels in er ii. Phys. Scr. **79**(4), 045301 (2009). https://doi.org/10.1088/0031-8949/79/04/045301
31. Q. Yu, X. Wang, Q. Li, Y. Li, Z. Dai, Experimental radiative lifetimes, branching fractions, and oscillator strengths of some levels in er i and er ii. Astrophys. J. Suppl. Ser. **240**(2), 25 (2019). https://doi.org/10.3847/1538-4365/aafb12
32. B.K. Ankush, M.N. Deo, Experimental verification of theoretical configuration mixing in the energy levels of er ii spectra via

isotope shift measurements using a fts. Am. J. Astron. Astrophys. **5**(2), 10–20 (2017). https://doi.org/10.11648/j.ajaa.20170502.11
33. Y. Naoi, M. Iwata, D. Yokota, G. Gaigalas, D. Kato, I. Murakami, H.A. Sakaue, Y. Sekiguchi, M. Tanaka, H. Tanuma, S. Wanajo, N. Nakamura, Laser induced breakdown spectroscopy of er ii for transition probability measurements. Appl. Sci. **12**(4), 2219 (2022). https://doi.org/10.3390/app12042219
34. S. Irvine, H. Andrews, K. Myhre, J. Coble, Radiative transition probabilities of neutral and singly ionized rare earth elements (la, ce, pr, nd, sm, gd, tb, dy, ho, er, tm, yb, lu) estimated by laser-induced breakdown spectroscopy. J. Quant. Spectrosc. Radiat. Transfer **297**, 108486 (2023). https://doi.org/10.1016/j.jqsrt.2023.108486
35. S. Morita, M. Goto, K. Nagaoka, C. Dong, H. Zhou, Z. Cui, Y. Dong, X. Gao, K. Ida, K. Ikeda, O. Kaneko, S. Lin, H. Nakano, M. Osakabe, R. Sakamoto, Y. Takeiri, A. Ti, K. Tsumori, M. Yoshinuma, L. group, Improvement of plasma performance using carbon pellet injection in large helical device. Plasma Sci. Technol **13**(3), 290 (2011). https://doi.org/10.1088/1009-0630/13/3/05
36. L.L. Lengyel, K. Büchl, G. Pautasso, L. Ledl, A.A. Ushakov, S. Kalvin, G. Veres, Modelling of impurity pellet ablation in asdex upgrade (neon) and wendelstein w7-as (carbon) by means of a radiative ('killer') pellet code. Nucl. Fusion **39**(6), 791 (1999). https://doi.org/10.1088/0029-5515/39/6/307
37. H.Y. Zhou, S. Morita, M. Goto, C.F. Dong, Zeff profile diagnostics using visible bremsstrahlung continuum for nonaxisymmetric plasmas with finite β in large helical device. J. Appl. Phys. **107**(5), 053306 (2010). https://doi.org/10.1063/1.3326970 https://pubs.aip.org/aip/jap/article-pdf/doi/10.1063/1.3326970/15050599/053306_1_online.pdf
38. M. Goto, S. Morita, M. Koubiti, Spectroscopic study of a carbon pellet ablation cloud. J. Phys. B: At. Mol. Opt. Phys. **43**(14), 144023 (2010). https://doi.org/10.1088/0953-4075/43/14/144023
39. W. Li, J. Grumer, T. Brage, P. Jönsson, Hfszeeman95–a program for computing weak and intermediate magnetic-field- and hyperfine-induced transition rates. Comput. Phys. Commun. **253**, 107211 (2020). https://doi.org/10.1016/j.cpc.2020.107211
40. A. Goly, S. Weniger, Stark widths and transition probabilities of some multiplets of singly ionized carbon. J. Quant. Spectrosc. Radiat. Transfer **28**(5), 389–391 (1982). https://doi.org/10.1016/0022-4073(82)90004-8
41. J.R. Roberts, K.L. Eckerle, Measurements of stark profiles of c ii and ca ii lines. Phys. Rev. **159**, 104–107 (1967). https://doi.org/10.1103/PhysRev.159.104
42. M.F. Gu, The flexible atomic code. Can. J. Phys. **86**(5), 675–689 (2008). https://doi.org/10.1139/p07-197
43. R.W.P. McWhirter, Spectral intensities, in *Plasma Diagnostic Techniques*. ed. by R.H. Hubblestone, S.L. Leonard (Academic Press, New York, 1965), p.201
44. G. Cristoforetti, A. De Giacomo, M. Dell'Aglio, S. Legnaioli, E. Tognoni, V. Palleschi, N. Omenetto, Local thermodynamic equilibrium in laser-induced breakdown spectroscopy:beyond the mcwhirter criterion. Spectrochim. Acta, Part B **65**(1), 86–95 (2010). https://doi.org/10.1016/j.sab.2009.11.005
45. S. Kodangil, N. Domoto, M. Tanaka, D. Kato, G. Gaigalas, H. Tanuma, N. Nakamura, Measurement of transition probabilities of la ii using laser induced breakdown spectroscopy (libs). J. Quant. Spectrosc. Radiat. Transfer **322**, 109011 (2024). https://doi.org/10.1016/j.jqsrt.2024.109011
46. H. Tanaka, K. Fujii, T. Shikama, S. Morita, M. Goto, M. Hasuo, Plasma spectroscopy on an aluminum-pellet ablation cloud in an LHD plasma with an echelle spectrometer. Atoms **8**(4), 81 (2020). https://doi.org/10.3390/atoms8040081
47. J.-F. Wyart, J. Blaise, W.P. Bidelman, C.R. Cowley, Energy levels and transition probabilities in doubly-ionized erbium (Er III). Phys. Scr. **56**(5), 446 (1997). https://doi.org/10.1088/0031-8949/56/5/008